Materials & Design 244 (2024) 113115

Contents lists available at ScienceDirect

Materials & Design

journal homepage: www.elsevier.com/locate/matdes

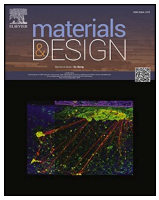

Contrastive learning based on hierarchical graph of microstructures through directed energy deposition process to establish process-structure–property relationship via autoencoder

Chengxi Chen [a,b], Stanley Jian Liang Wong [a,b], Eddie Zhi'En Tan [b], Hua Li [a,*]

[a] Singapore Centre for 3D Printing, School of Mechanical and Aerospace Engineering, Nanyang Technological University, 50 Nanyang Avenue, Singapore 639798, Singapore
[b] Makino Asia Pte Ltd, 2 Gul Avenue, Singapore 629649, Singapore

ARTICLE INFO

Keywords:
Contrastive learning
Hierarchical graph
Electron backscatter diffraction (EBSD)
Process-structure–property
Directed energy deposition (DED)

ABSTRACT

n this study, an innovative algorithm is developed to transform microstructures to hierarchical graphs without manual feature engineering. The hierarchical graph comprises two layers. Initially, pixel data, which includes Euler angles, phase, and position, forms the pixel-wise graphs within individual grains. Following this foundation, the grains serve as nodes, constituting the second layer. Importantly, the hierarchical graph preserves essential measurement data and structural details for training machine learning models. After that, a contrastive learning model based on hierarchical graph is designed to capture representations of microstructures obtained by the electron backscatter diffraction (EBSD) technique. This model can be directly extended for other microscopy techniques, such as Scanning Electron Microscopy (SEM), Energy-Dispersive X-ray spectroscopy (EDX), and Transmission Electron Microscopy (TEM). Using the learned microstructure representations, an autoencoder model for the directed energy deposition (DED) is developed to establish the relationship among process parameters, microstructures, and material properties, completing the process-structure–property cycle quantitatively. The performance of the present model is naturally benchmarked against two other models: a contrastive learning model based on pixel-wise graph (without manual feature engineering) and a contrastive learning model based on grain-wise graph (employing manual feature engineering). The results of the present model highlight the potential in decoding the process-structure–property relationships in the DED process.

1. Introduction

Laser powder-based directed energy deposition (DED) has seen rapidly growth in the manufacturing industry, drawing much interest from numerous domains [1]. Complex physical phenomena occur in the deposition process and have a significant influence on performance and hinder development [2]. It is essential to establish the relationship among the process parameters, microstructures, and properties for boosting the DED process development [1,3–7]. Within this relationship, microstructures are of paramount importance. Yet, incorporating microstructures into this relationship is challenging.

Two primary methodologies to explore microstructures are through experimentation and modeling. Experimental techniques, such as Focused Ion Beam (FIB), Scanning Electron Microscopy (SEM), Energy-Dispersive X-ray spectroscopy (EDX), Electron Backscatter Diffraction (EBSD), Transmission Electron Microscopy (TEM), Atomic Force Microscopy (AFM), Atom Probe Tomography (APT), and X-ray Diffraction (XRD), offer direct microstructural characterization. This data is then employed to discern qualitative relationships ranging from process parameters to microstructures [8], from microstructures to properties [9–11], from process parameters to properties [12–16], and among process parameters, microstructures, and properties [17–23]. However, experiments can only establish qualitative process-structure–property relationship within specific experimental settings.

Alternatively, On the other hand, physics-based modeling delivers a quantitative method for simulating microstructures [24–49]. It encompasses modeling aspects like powder stream, heat source, melt pool, and solidification events in the DED process [50]. Yet, this approach has its pitfalls: it's computationally demanding [51] and intricacies arise due to the various physical processes involved [52], not to mention the

* Corresponding author.
E-mail address: lihua@ntu.edu.sg (H. Li).

https://doi.org/10.1016/j.matdes.2024.113115
Received 22 April 2024; Received in revised form 4 June 2024; Accepted 23 June 2024
Available online 24 June 2024
0264-1275/© 2024 The Authors. Published by Elsevier Ltd. This is an open access article under the CC BY license (http://creativecommons.org/licenses/by/4.0/).

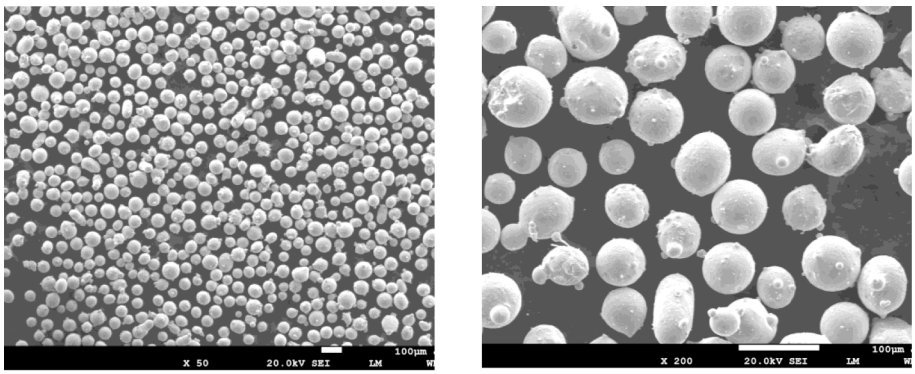

Fig. 1. SEM image of SS316L powder (a) 50× (b) 200×.

challenges of integrating process parameters, microstructures, and properties through multi-scale multi-physics modeling [53,54]. However, physics-based simulations are computationally demanding and become intricate due to the involvement of various physical processes.

To address these challenges, machine learning (ML) has been introduced as a potential solution. Li *et al.* utilized an artificial neural network (ANN) to explore the relationship between the grain boundary tilt angle and three influencing factors: thermal gradient, crystal orientation, and the Marangoni effect [55]. Han *et al.* introduced a deep learning framework designed for the quantitative assessment of metal microstructural changes fabricated by AM under varying conditions. The primary microstructural descriptors were directly drawn from the EBSD patterns. They showcased their model's proficiency in forecasting new microstructures within the representational domain, employing a regeneration neural network [56]. Cooper *et al.* adopted a deep convolutional generative adversarial network (DC-GAN) to produce authentic phase microstructural information [57]. Furthermore, they pioneered the SliceGAN architecture, a generative adversarial network capable of creating high-resolution 3D datasets using a single illustrative 2D image [58]. Xue *et al.* put forth a physics-integrated graph network. This approach ingeniously employed a graph depiction of the grain structure, integrating conventional phase field theory into the graph network. It addressed temperature field, liquid/solid phase ratio, and grain orientation variables to minimize a physics-centric loss/energy function [41]. Yan *et al.* utilized data-mining methods to complete the cycle of design, prediction, and optimization. This was grounded in extensive material modeling that linked process, structure, and property relationships for AM materials [53,54]. Fang *et al.* used a 1D convolutional neural network to forecast mechanical properties based on simulated thermal history. They analyzed the simulated thermal process data, microstructure, and recorded mechanical properties to understand the process-structure–property relationship [59]. However, to the best of our knowledge, microstructure modeling using machine learning without feature engineering and integrating microstructure into the interplay of process parameters, microstructures, and properties to establish the process-structure–property relationship in the DED process remains unexplored.

Microstructure data obtained via EBSD can be treated as images, but this approach has several shortcomings. Firstly, the images contain only red, green, and blue (RGB) information, which varies based on different software and settings. Secondly, the images need to be preprocessed to a uniform size for machine learning. Thirdly, the dataset is much smaller in number and larger in size compared to the average 500–1000 clean, full-resolution images of 350 × 400 pixels from ImageNet. The larger image size increases the requirements for machine learning training. Due to these shortcomings, it is unfeasible to apply machine learning directly to these images. Therefore, an innovative algorithm was developed to transform microstructures into graphs. Graphs offer several advantages. Digital values can be stored in each node as node features without any loss of information. Additionally, graph nodes do not need to be aligned to the same size, and graphs can be trained individually or in multiples using graph neural networks. In this paper, an innovative algorithm is developed to transform microstructures to hierarchical graph. After that, a contrastive learning model based on hierarchical graph is proposed to learn the representation of microstructures obtained by EBSD technique without feature engineering. By the learned microstructure representations, an autoencoder model for DED process is proposed to establish the relationship among process parameters, microstructure, and properties by adding extra loss function between the normalized learned representation of microstructures and the latent variables from the autoencoder architecture.

Table 2
Particle size distribution of SS316.

Sieve (μm)	−45	+45	+53	+63	+75	+90
Wt%	2.00	13.50	27.10	35.00	19.50	2.90

In the following section, an initial introduction is provided on the experimental design, procedure and results related process parameters, microstructures, and properties. Section 3 presents a contrastive learning based hierarchical graph for learning the representation of microstructures in DED process. Section 4 leverages an autoencoder model to establish the relationship among process parameters, microstructure, and properties (AE4PSP). Section 5 presents the results and discussion. Finally, the conclusion drawn from the current study is discussed in Section 6.

2. Experimental setup and results

2.1. Experimental procedure

The alloy deposited is SS316L (DM 3D-316L) from Dura-Metal North America Corporation with a powder composition by weight percentage of Fe-17Cr-12Ni-2.5Mo for the entire experiments. The SEM images of

Table 1
Chemical composition of SS316L.

Composition	Fe	Cr	Ni	Mo	Si	Mn	O	C	P
Wt%	Bal.	16.27	13.9	2.71	0.85	0.25	0.082	0.049	0.013

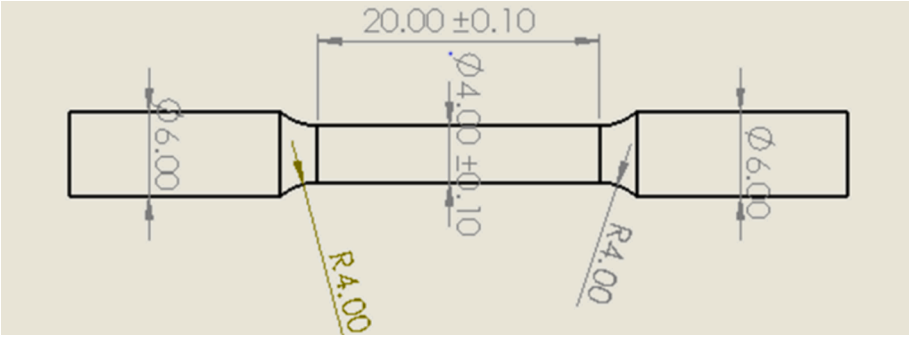

Fig. 2. Dimension of specimens for tensile test.

SS316L powder are shown in Fig. 1. The chemical composition of SS316L powder used for this investigation is shown in Table 1, and particle size distribution of the powder is shown in Table 2.

The DED process is conducted by a BeAM 800 Magic DED machine (see machine specification in Supplementary materials Table S1), employing the process parameters mentioned before, where the alternating scan angle of 90° is imposed between printed layers. After the deposition process, the printed parts, as shown in Fig. 3 (a), are carefully detached from the substrate using a Troop wire cut machine shown in Fig. 3 (b), minimizing damage and distortion to the specimens. A portion of the block material is then fabricated into tensile test specimens conforming to specimen 4 from ASTM E8 [60] small-size specimen proportional to standard in Fig. 2.

The remaining cut specimens are then mounted with Polyfast conductive resin, providing proper electrical conductivity and stability during subsequent microstructure acquisition steps. The mounted samples undergo a series of grinding and polishing stages by Struers as shown in Fig. 3 (c) to achieve a mirror-like finish. Initially, 320 grit sandpaper is used for grinding to remove surface irregularities and attain a flat surface. The specimens are then polished sequentially with 9 μm and 3 μm diamond suspensions to eliminate scratches and smoothen the surface. Final polishing is performed using a 1 μm Oxide Polishing Suspension (OPS), resulting in a surface suitable for advanced microscopy analyses. Furthermore, the polished specimens are examined using a JEOL 7800F Prime Field Emission Scanning Electron Microscope (FSEM), equipped with a Symmetry EBSD detector as shown in Fig. 3 (d). Suitable imaging and data acquisition conditions, including accelerating voltage (20 KV), work focus distance (20 mm), mode 2, exposure time (0.3 ms) and step size (2 μm), are selected to obtain high-quality EBSD data.

Porosity analysis is carried out using a Keyence VHX-7000 optical microscope shown in Fig. 3 (e), with appropriate magnification (200 ×) and imaging conditions chosen to capture representative images of the specimens. Image analysis techniques are employed to calculate porosity percentage and characterize the pore size distribution and morphology. The tensile test is performed using a Shimadzu testing machine shown in Fig. 3 (h) with a 10 kN load capacity. Prior to testing, the tensile coupons are painted black and marked with two white lines shown in Fig. 3 (g) to enhance contrast for accurate strain measurement using a video extensometer shown in Fig. 3 (h). Vicker hardness measurement is conducted by Wilson-VH3100 shown in Fig. 3 (f).

2.2. Design of experiments

The DED process involves different process parameters, classified into laser, feeding, material & design, and scanning strategy [3]. The laser power, the scanning speed, and the powder mass flow rate, *XY*-incremental ratio, *Z*-incremental ratio are significant parameters affecting microstructure, defects (cracks, porosity), geometrical characteristics, and mechanical properties [3,5,61]. Therefore, these parameters are chosen as the printing parameters in this research. For design of experiments (DOE), 54-run experiments by the response surface methodology (RSM) and 20-run full factorial design experiments are carried out for modeling of process parameters, microstructure, and properties. The ranges of process parameters for the RSM and full factorial design are shown in Table 3 and Table 4 separately.

The process parameters have been meticulously chosen. By default, the maximum laser power is set at 2,000 w, and the highest powder mass flow rate is 22 g/min. Using the standard parameters provided for SS316L, the central point for the RSM in this experiment is established with a laser power of 1,300 w, scanning speed of 1,800 mm/min, powder mass flow rate of 16 g/min, an *XY*-incremental Ratio of 0.6, and a *Z*-incremental Ratio of 1.3. It's worth noting that the *XY*-incremental Ratio represents the width ratio of a single-track deposition, while the *Z*-incremental Ratio signifies its height ratio.

For the RSM factorial points, the laser power is set between 1,000 and 1,600 w, scanning speeds range from 1,600 to 2,000 mm/min, powder mass flow rates vary between 14 and 18 g/min, *XY*-incremental Ratios are between 0.5 and 0.7, and *Z*-incremental Ratios lie between 1.2 and 1.4. Owing to the default alpha value of 1.633, the RSM experimental ranges cover laser power from 810 to 1,790 w, scanning speeds from 1,437 to 2,127 mm/min, powder mass flow rates from 12.7 to 19.3 g/min, *XY*-incremental Ratios from 0.44 to 0.76, and *Z*-incremental Ratios from 1.07 to 1.73.

Subsequently, the full factorial design's factorial points have been set: laser power ranges from 1,400 to 1,800 w, scanning speeds between 2,000 and 3,000 mm/min, powder mass flow rates from 16 to 20 g/min, *XY*-incremental Ratios of 0.4 and 0.6, and *Z*-incremental Ratios of 1.2 and 1.4.

2.3. Experimental results

The inverse pole figure (IPF) maps of EBSD are presented in Table S2 (see Supplementary materials). The experimental results including yield strength, ultimate tensile strength (UTS), elongation at break, Young's modules, porosity, and hardness of RSM and full factorial design are shown in Table 5 and Table 6 separately.

3. Development of algorithm for transforming microstructures to graphs

The microstructure data for this study is collected through an EBSD montage with a 5 mm × 5 mm area using Aztec. The fields are aligned using an L-shaped "Guided Align" approach, followed by data montage and export to an h5oina format. The h5oina file is then imported into AZtecCrystal for further processing. Initial data cleanup involves removing wild spikes and applying a five-neighbors zero-solution removal. After the cleanup process, an EBSD grid mapping consists of m rows and n columns of pixels. Each pixel, measuring 2 μm × 2 μm, is treated as a node with attributes including pixel ID, grain ID, phase, Euler angles ("phi1," "Phi," "phi2"), and position (x, y). The total number of pixel nodes, N, is approximately 6,250,000, as indicated in

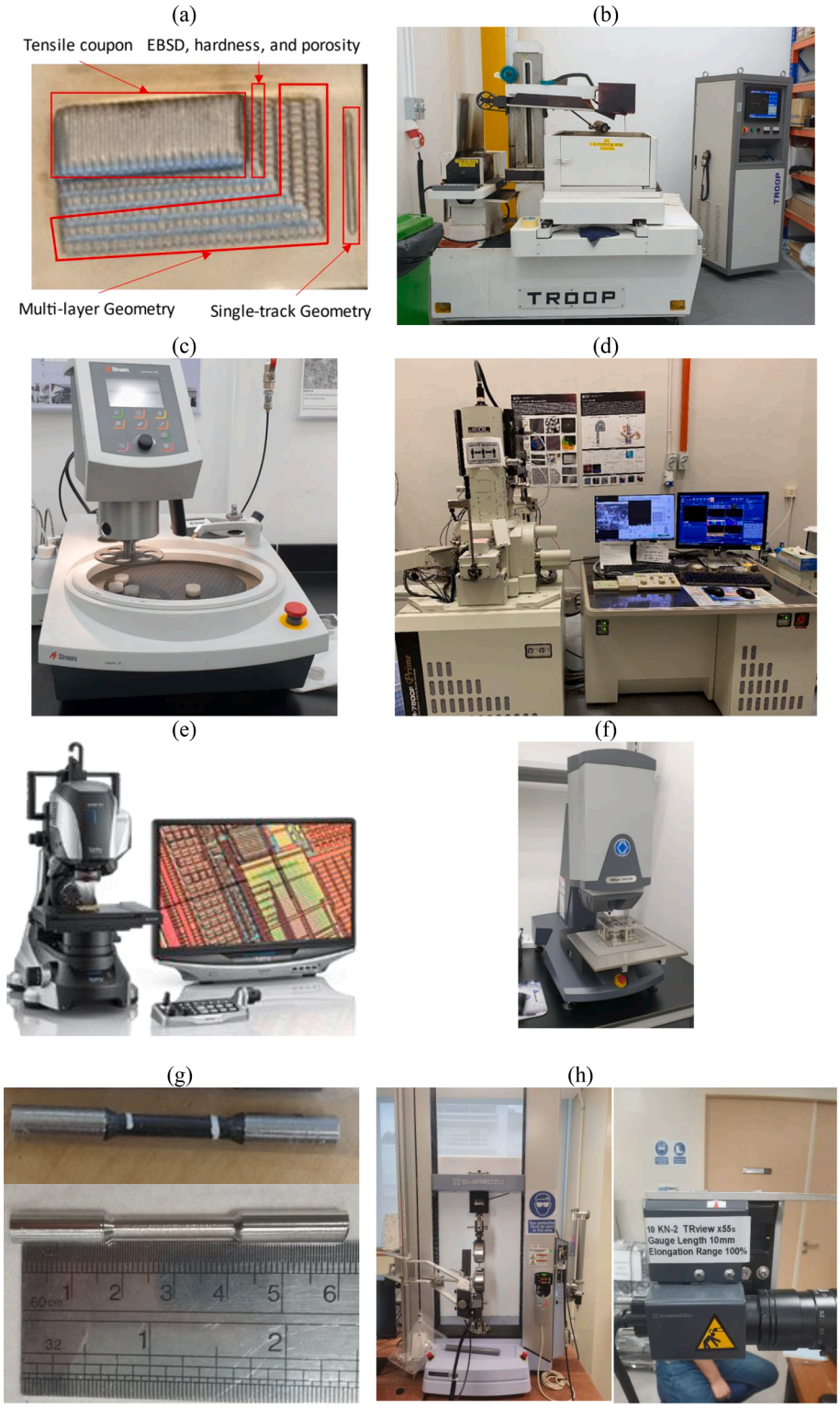

Fig. 3. Sample preparation (a) printed part, (b) Troop wire cut machine, (c) Struers Tegramin 25, (d) JOEL FESEM 7800F, (e) Keyence VHX-7000, (f) Wilson-VH3100, (g) tensile coupon, (h) Shimadzu tensile tester.

equation (1). Edges are then established between neighboring pixels, forming an adjacency matrix $A_{pixel} \in \mathbb{R}^{N\times N}$, which creates a pixel-wise graph, as illustrated in Fig. 4 (b).

$$N = m \times n \in R \tag{1}$$

Given that the grain ID of each pixel is known, one-hot encoding can be applied to the N pixels to generate $A_{pixel2grain} \in \mathbb{R}^{N\times K}$, where K represents the total number of grains. In this representation, each grain is treated as a node composed of its constituent pixels, thereby reducing the number of nodes from millions to thousands. The adjacency matrix of the grain graph is derived using equation (2), resulting in a hierarchical graph without the need for manual feature engineering, as shown in Fig. 4 (a). In contrast to a single, comprehensive pixel-wise graph, a hierarchical graph comprises K pixel-wise graphs, each corresponding to a different

Table 3
RSM.

Control factors	Level 1	Level 2	Level 3
Laser power (W)	1,000	1,300	1,600
Scanning speed (mm/min)	1,600	1,800	2,000
Powder flow rate (g/min)	14	16	18
XY-incremental Ratio	0.5	0.6	0.7
Z-incremental Ratio	1.2	1.3	1.4

Table 4
Full factorial design.

Control factors	Level 1	Level 2
Laser power (W)	1,400	1,800
Scanning speed (mm/min)	2,000	3,000
Powder flow rate (g/min)	16	20
XY-incremental Ratio	0.4	0.6
Z-incremental Ratio	1.2	1.4

grain. These can be learned simultaneously in parallel as features for grains.

$$A_{grain} = A_{pixel2grain}{}^{T} A_{pixel} A_{pixel2grain} \in \mathbb{R}^{K\times K} \tag{2}$$

Alternatively, a "Grain Size" analysis is conducted in AZtecCrystal using manual feature engineering. During this process, grain features such as aspect ratio, centroid (x, y), ellipse angle, ellipse length, mean Euler angles ("phi1," "Phi," "phi2"), and phase are extracted and prepared for the grain graph, as illustrated in Fig. 4 (c). An example of transforming microstructures into a grain-wise graph is shown in Fig. 5.

After applying the developed algorithm to transform microstructures into hierarchical graphs, these graph representations enhance the analysis and modeling of the microstructure using graph-based models. Additionally, this approach allows for a natural comparison between pixel-wise and grain-wise graphs.

4. Development of contrastive learning model based on hierarchical graph

4.1. Premise of graph neural network and contrastive learning

Graph Neural Networks (GNNs) are a class of deep learning models specifically designed to handle graph-structured data. By exploiting the relational information between nodes in a graph, GNNs can effectively capture complex patterns in data with inherent graph structures. In material science, microstructures can be naturally represented as graphs, where nodes correspond to individual grains or phases, and edges represent grain boundaries or phase interfaces. The relationships between various microstructural features, such as grain size, grain orientation, and phase distribution, can be captured through the graph representation. Traditional machine learning techniques often struggle with irregular data and complex relationships found in microstructures. However, GNNs are specifically designed to handle such data by exploiting the relational information between nodes in a graph. They can learn both local and global patterns in the microstructure, providing a powerful means to predict material properties based on the underlying graph structure.

The Graph Isomorphism Network (GIN) [62] is advantageous over other GNN variants as it is more powerful in distinguishing between different graph structures and can better capture the subtleties in graph-structured data. This makes it well-suited for tasks such as microstructure modeling, where the intricate relationships between nodes (grains or phases) and edges (grain boundaries or phase interfaces) are of utmost importance.

Contrastive learning is a self-supervised learning approach that aims to learn meaningful representations of data by optimizing a model to discriminate between similar and dissimilar data points. This is achieved by training the model to maximize the similarity between semantically related (positive) pairs while minimizing the similarity between unrelated (negative) pairs. The idea is that by learning to recognize the differences between positive and negative pairs, the model learns to encode meaningful and discriminative features in the data. In the case of graphs, positive pairs can be generated by subgraph sampling, node reordering, or adding/removing edges, while negative pairs can be obtained by sampling unrelated graphs or randomly shuffling the graph structure. A GNN is trained to learn node or graph representations that maximize the similarity between the positive pairs and minimize the similarity between the negative pairs. Simple Siamese (SimSiam) [63] is a self-supervised learning method that uses contrastive learning principles for learning representations. However, unlike traditional contrastive learning methods, SimSiam does not require negative pairs. Instead, it learns representations by maximizing the similarity between two differently augmented views of the same data point. SimSiam has shown promising results in various self-supervised learning tasks, achieving competitive performance compared to other contrastive learning methods, despite not using negative pairs. This makes SimSiam an attractive option for representation learning, especially when computational resources or labeled data are limited.

4.2. Development of contrastive learning based on hierarchical graph

In this research, we develop a hierarchical graph based contrastive learning (HGCL) model that adopts SimSiam as framework and uses hierarchical GNN as backbone, illustrated in Fig. 6, to learn representations of microstructures derived from EBSD data. The EBSD data is transformed into pixel-based and grain-based graphs, which are then divided into two distinct views. The hypothesis is that if a sufficient number of tracks are measured using EBSD from the same set of process parameters, the resulting two views derived from the same EBSD data should show similarity. To test this hypothesis, an area of 5 mm by 5 mm is analyzed using EBSD. The model is designed to learn representations by maximizing the similarity between the two different views of the same EBSD data.

The underlying GNN architecture employed in this framework is GIN. The update rule for GIN, expressed through the message-passing framework, can be described as follows:

$$x_i^{k+1} = MLP^k\left((1+\varepsilon)\bullet x_i^k + \sum_{j\in N(i)} x_j^k\right) \tag{3}$$

Where x_i^k is node i feature of layer k, MLP is a multilayer perceptron, x_j^k is the feature of node j which is the neighbor of node i, ε is a learnable parameter.

Two linear encoders (f) that share the same architectures and weights encode the readout of GIN from two views.

$$z_i = f_\Psi\left(x_i'\right) \tag{4}$$

$$z_j = f_\Psi\left(x_j'\right) \tag{5}$$

Where z_i is the readout from view 1, z_j is the readout from view 2.

Then a predictor network (h) that is used to create an intermediate prediction from one of the encoders.

$$p_i = h(z_i) \tag{6}$$

Table 5
Design matrix and properties results of RSM.

Sample No.	Laser power (W)	Scanning speed (mm/min)	Powder mass flow rate (g/min)	*XY*-incremental Ratio	*Z*-incremental Ratio	Yield Tensile Strength (MPa)	UTS (MPa)	Elongation (%)	Young's Modulus (GPa)	Porosity (0.01 %)	Hardness (HV)
1	1,000	1,600	14	0.5	1.2	497	670	47	152	60	215
2	1,600	2,000	14	0.5	1.2	453	644	23	148	14	221
3	1,600	1,600	18	0.5	1.2	414	610	41	127	57	200
4	1,000	2,000	18	0.5	1.2	490	664	44	157	83	217
5	1,600	1,600	14	0.7	1.2	449	636	25	146	40	214
6	1,000	2,000	14	0.7	1.2	469	642	47	133	12	219
7	1,000	1,600	18	0.7	1.2	448	627	24	140	178	211
8	1,600	2,000	18	0.7	1.2	493	654	28	55	2	217
9	1,600	1,600	14	0.5	1.6	415	589	17	128	68	202
10	1,000	2,000	14	0.5	1.6	449	647	56	165	20	217
11	1,000	1,600	18	0.5	1.6	421	591	29	118	134	208
12	1,600	2,000	18	0.5	1.6	449	644	38	153	11	214
13	1,000	1,600	14	0.7	1.6	477	649	32	142	238	209
14	1,600	2,000	14	0.7	1.6	431	624	27	148	20	227
15	1,600	1,600	18	0.7	1.6	438	633	45	146	44	206
16	1,000	2,000	18	0.7	1.6	492	655	36	136	126	232
17	1,300	1,800	16	0.6	1.4	451	644	40	164	65	212
18	1,300	1,800	16	0.6	1.4	425	635	36	134	7	215
19	1,300	1,800	16	0.6	1.4	444	646	47	135	39	208
20	1,300	1,800	16	0.6	1.4	459	656	34	142	27	207
21	1,600	1,600	14	0.5	1.2	401	592	25	130	28	206
22	1,000	2,000	14	0.5	1.2	451	637	50	103	41	219
23	1,000	1,600	18	0.5	1.2	434	638	41	154	131	208
24	1,600	2,000	18	0.5	1.2	419	637	34	141	13	211
25	1,000	1,600	14	0.7	1.2	447	641	38	142	102	212
26	1,600	2,000	14	0.7	1.2	486	649	53	163	3	232
27	1,600	1,600	18	0.7	1.2	432	625	32	139	65	211
28	1,000	2,000	18	0.7	1.2	460	648	47	162	228	220
29	1,000	1,600	14	0.5	1.6	468	645	38	111	44	211
30	1,600	2,000	14	0.5	1.6	377	609	37	120	25	240
31	1,600	1,600	18	0.5	1.6	361	591	30	113	70	203
32	1,000	2,000	18	0.5	1.6	490	664	34	154	90	218
33	1,600	1,600	14	0.7	1.6	416	613	26	135	14	212
34	1,000	2,000	14	0.7	1.6	448	617	25	132	6	223
35	1,000	1,600	18	0.7	1.6	474	646	25	131	63	245
36	1,600	2,000	18	0.7	1.6	445	642	41	102	9	214
37	1,300	1,800	16	0.6	1.4	429	636	50	130	20	213
38	1,300	1,800	16	0.6	1.4	–	–	–	–	–	–
39	1,300	1,800	16	0.6	1.4	–	–	–	–	–	–
40	1,300	1,800	16	0.6	1.4	–	–	–	–	–	–
41	810.1	1,800	16	0.6	1.4	506	656	29	143	1.8	211
42	1,790	1,800	16	0.6	1.4	413	606	21	143	0.1	205
43	1,300	1,473	16	0.6	1.4	421	626	43	105	0.2	211
44	1,300	2,127	16	0.6	1.4	417	609	35	126	0.5	220
45	1,300	1,800	12.7	0.6	1.4	410	613	31	137	0.1	216
46	1,300	1,800	19.3	0.6	1.4	418	601	36	115	1	212
47	1,300	1,800	16	0.44	1.4	426	643	45	135	0.3	211
48	1,300	1,800	16	0.76	1.4	445	642	37	136	0.1	218
49	1,300	1,800	16	0.6	1.07	436	650	38	153	0.4	214
50	1,300	1,800	16	0.6	1.73	385	595	45	112	0.4	211
51	1,300	1,800	16	0.6	1.4	–	–	–	–	–	–
52	1,300	1,800	16	0.6	1.4	–	–	–	–	–	–
53	1,300	1,800	16	0.6	1.4	–	–	–	–	–	–
54	1,300	1,800	16	0.6	1.4	–	–	–	–	–	–

$$p_j = h(z_j) \tag{7}$$

The symmetric loss function used in SimSiam is the negative cosine similarity between the output of the predictor network (p_i or p_j) and the output of the other encoder (z_i or z_j):

$$Loss = -\left(\frac{p_i \bullet z_j^T}{\|p_i\| \bullet \|z_j\|} + \frac{p_j \bullet z_i^T}{\|p_j\| \bullet \|z_i\|}\right) \Big/ 2 \tag{8}$$

Beside HGCL, another two variants, namely pixel-wise graph based contrastive learning (PGCL), grain-wise graph based contrastive learning (GGCL), are chosen as benchmark models. The advantage of the PGCL is its end-to-end learning capability without requiring any feature engineering. However, this approach encompasses millions of nodes, resulting in a high computational cost and inability to capture grain-level information. On the other hand, GGCL significantly reduces the node count from millions to a few thousands. This approach, however, necessitates feature engineering to define grain parameters such as aspect ratio, centroid (x, y), ellipse angle, ellipse long, mean Euler angle ("phi1", "Phi", "phi2"), and phase.

5. Development of autoencoder model for process parameters, microstructures, and properties (AE4PSP)

5.1. Data preprocessing

Given the limited size of the available data, a design of experiments (DOE) informed deep learning methodology [64] is employed to

Table 6
Design matrix and properties results of full factorial design.

Sample No.	Laser power (W)	Scanning speed (mm/min)	Powder mass flow rate (g/min)	*XY*-incremental Ratio	*Z*-incremental Ratio	Yield Strength (MPa)	UTS (MPa)	Elongation (%)	Youg's Modulus (GPa)	Porosity (0.01 %)	Hardness (HV)
1	1,400	2,000	16	0.4	1.4	453	635	43	96	13	208
2	1,800	2,000	16	0.4	1.2	420	616	27	124	4	200
3	1,400	3,000	16	0.4	1.2	436	616	40	139	18	211
4	1,800	3,000	16	0.4	1.4	426	623	27	102	23	209
5	1,400	2,000	20	0.4	1.2	451	638	36	132	61	213
6	1,800	2,000	20	0.4	1.4	415	608	36	125	15	213
7	1,400	3,000	20	0.4	1.4	428	627	44	129	22	212
8	1,800	3,000	20	0.4	1.2	427	633	35	136	11	207
9	1,400	2,000	16	0.6	1.2	459	646	48	124	130	216
10	1,800	2,000	16	0.6	1.4	435	617	30	145	7	209
11	1,400	3,000	16	0.6	1.4	424	603	35	115	50	209
12	1,800	3,000	16	0.6	1.2	471	639	27	157	8	211
13	1,400	2,000	20	0.6	1.4	474	652	37	139	107	210
14	1,800	2,000	20	0.6	1.2	401	572	31	93	30	209
15	1,400	3,000	20	0.6	1.2	425	621	55	124	24	206
16	1,800	3,000	20	0.6	1.4	444	634	31	124	11	216
17	1,600	2,500	18	0.5	1.3	418	620	25	122	15	209
18	1,600	2,500	18	0.5	1.3	417	620	40	91	40	205
19	1,600	2,500	18	0.5	1.3	438	631	29	125	18	212
20	1,600	2,500	18	0.5	1.3	453	651	37	177	22	197

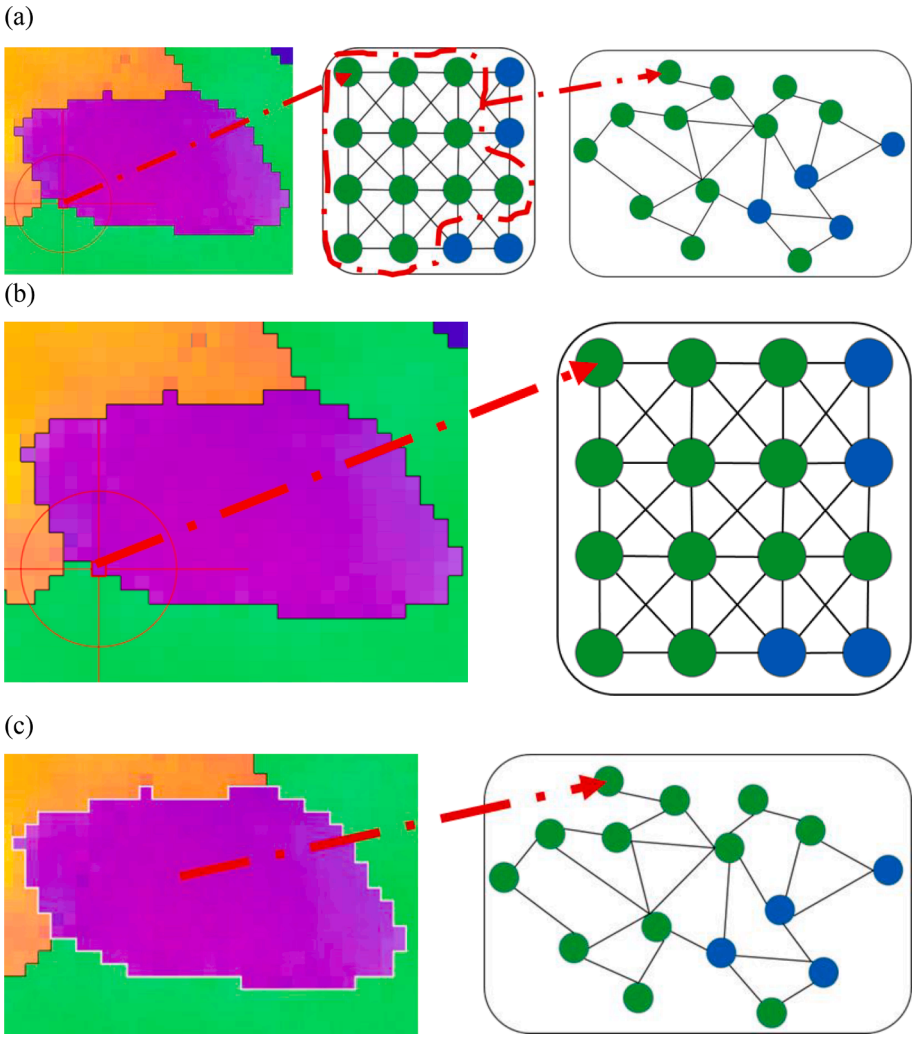

Fig. 4. Variants of graphs (a) hierarchical graph (b) pixel-wise graph (c) grain-wise graph.

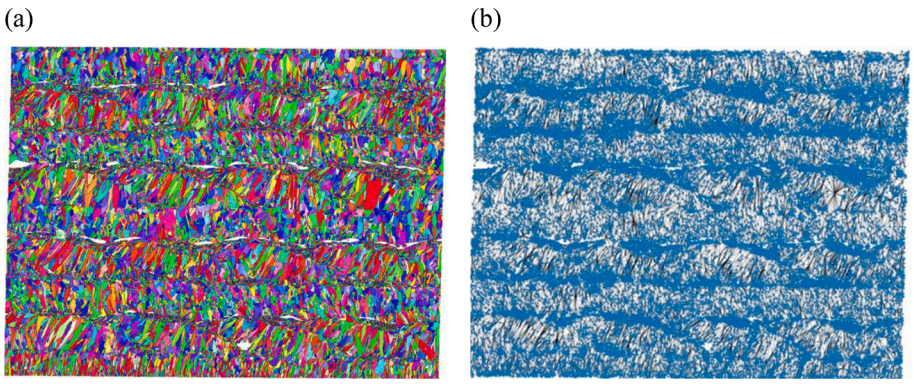

Fig. 5. Transforming microstructures to graph (a). EBSD inverse pole figure, (b) grain-wise graph.

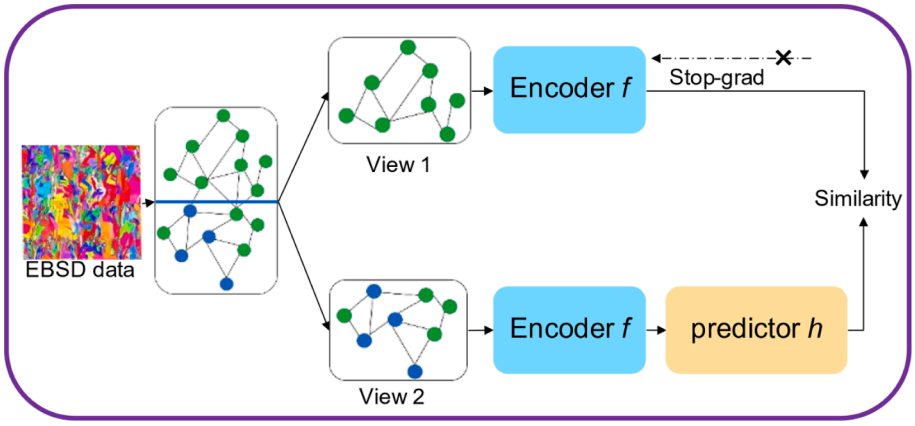

Fig. 6. Architecture of graph based contrastive learning.

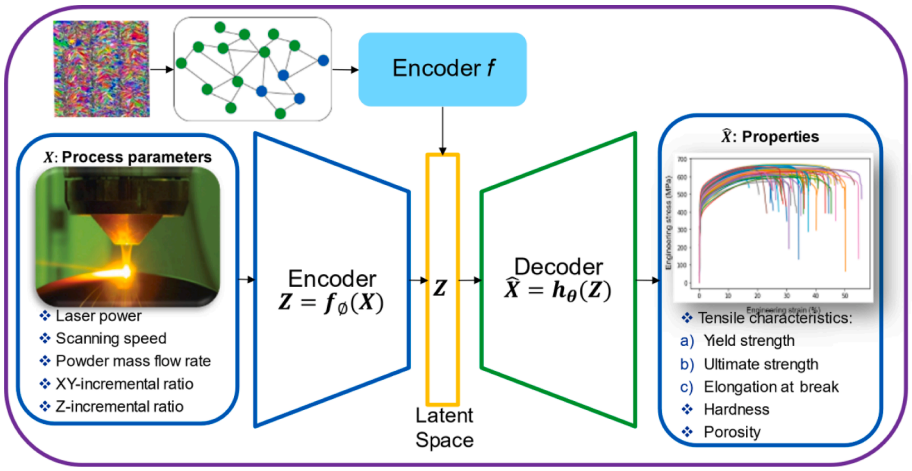

Fig. 7. Architecture of AE4PSP model.

augment the dataset. First, 16-dimensional latent variables of 67 experimental runs are predicted by the graph-based contrastive learning. Next, the augmentation process is applied to map process parameters to latent variables and process parameters to properties. Subsequently, the pretraining process is conducted using the augmented dataset. Finally, the pretrained model is fine-tuned with the experimental dataset to obtain a robust and well-generalized model capable of handling complex process parameters, microstructures, and properties relationships.

5.2. AE4PSP model development

The graph-based contrastive learning models learn to extract meaningful and invariant features that can be used as latent variables to link process parameters and properties in the proposed autoencoder architecture, as shown in Fig. 7.

$$\widetilde{Z} = f_{\Psi}(MLP_{\Theta}((A + (1+\varepsilon) \bullet I) \bullet X')) \tag{9}$$

In Fig. 7, process parameters including laser power, scanning speed, powder mass flow rate, *XY*-incremental ratio, and *Z*-incremental ratio

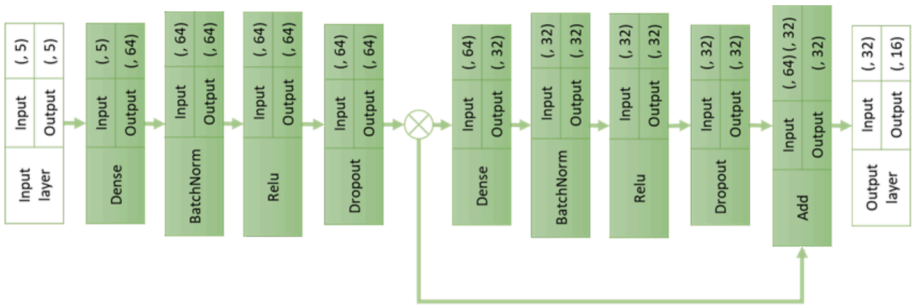

Fig. 8. Architecture of the encoder.

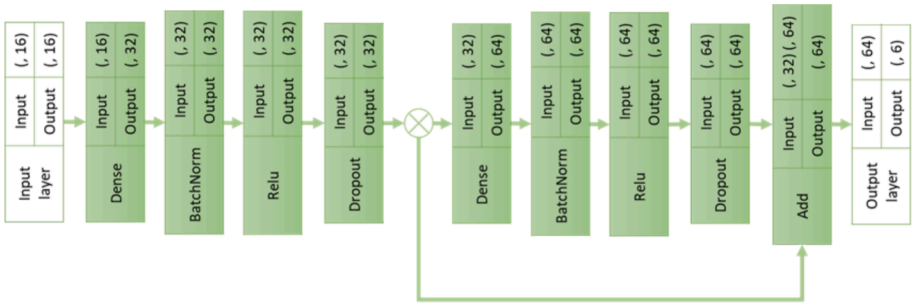

Fig. 9. Architecture of the decoder.

are passed through encoder to get latent variables.

$$Z = f_{\varnothing}(X) \tag{10}$$

The architecture of the encoder starts with an input layer with five dimensions representing laser power, scanning speed, powder mass flow rate, XY-incremental ratio, and Z-incremental ratio. It follows a dense layer to upscale the dimension from 5 to 64, then followed by BatchNorm, ReLu, and Dropout layers. The outputs from the previous block are then passed on to one more set of layers where each set consists of a dense layer, a BatchNorm, a ReLu, a Dropout layer, and a residual layer to downscale the dimension to 32. Finally, the predicted latent variables are reduced to 16 dimensions, as shown in Fig. 8.

Then latent variables are decoded into properties including yield strength, ultimate tensile strength, elongation at break, porosity, and hardness.

$$\widehat{X} = h_{\theta}(Z) \tag{11}$$

The architecture of the decoder is a symmetrical architecture of encoder, which starts from the 16-dimensional latent variables, upscaling the dimension from 16 to 32, then followed by BatchNorm, ReLu, and Dropout layers. The outputs from the previous block are then passed on to one more set of layers where each set consists of a dense layer, a BatchNorm, a ReLu, a Dropout layer, and a residual layer to upscale the dimension to 64. Finally, the predicted variables are the properties with 6 dimensions, as shown in Fig. 9.

The loss function during the training is as follows:

$$Loss = \lambda \bullet \|Z - \widetilde{Z}\|^2 + (1-\lambda) \bullet \|\widehat{X}^{'} - \widehat{X}\|^2 \tag{12}$$

The trained model possesses the capability to predict properties in three distinct setups: predicting properties directly from process parameters without involving microstructure characteristics, as presented in this study; predicting properties from microstructure characteristics without considering process parameters; and predicting properties by using both process parameters and microstructure characteristics, with the latter's representation being concatenated by ratio. Therefore, the process-structure–property loop is completed in forward way, either from process parameters to properties, or from microstructure characteristics to properties.

Table 7
MAPE and RMSE results.

	Grain AE4PSP		Pixel AE4PSP		Hierarchical AE4PSP	
	MAPE	RMSE	MAPE	RMSE	MAPE	RMSE
Yield strength (MPa)	0.052	29.8	0.052	29.3	0.050	29.7
UTS (MPa)	0.030	22.1	0.030	22.8	0.030	22.0
Elongation (%)	0.189	8.7	0.201	8.8	0.212	9.3
Young's modules (GPa)	0.210	27.3	0.211	27.7	0.21	27.2
Porosity (%)	2.210	0.30	2.623	0.29	2.356	0.29
Hardness (HV)	0.032	8.24	0.033	8.53	0.034	8.76

6. Results and discussion

Evaluating the performance of representation learning doesn't have a straightforward method. Thus, assessing the accuracy of downstream tasks is employed. The downstream task is to predict yield strength, ultimate tensile strength, elongation at break, porosity, and hardness.

The Mean Absolute Percentage Error (MAPE) and Root Mean Squared Error (RMSE) are selected as the regression metrics to evaluate the performance of models. If $\hat{y}_i$ is the predicted value of the i-th sample and is the corresponding true value, then the MAPE estimated over is defined as:

$$MAPE(y, \hat{y}) = \frac{1}{N}\sum_{i=0}^{N-1}\frac{|y_i - \hat{y}_i|}{\max(\varepsilon, |y_i|)} \tag{13}$$

The RMSE is defined as:

$$RMSE(y, \hat{y}) = \sqrt{\frac{1}{n}\sum_{j=1}^{n}\left(y_j - \hat{y}_j\right)^2} \tag{14}$$

Table 7 and Fig. 10 illustrate that grain AE4PSP, pixel AE4PSP, and hierarchical AE4PSP exhibit similar performance. This indicates that

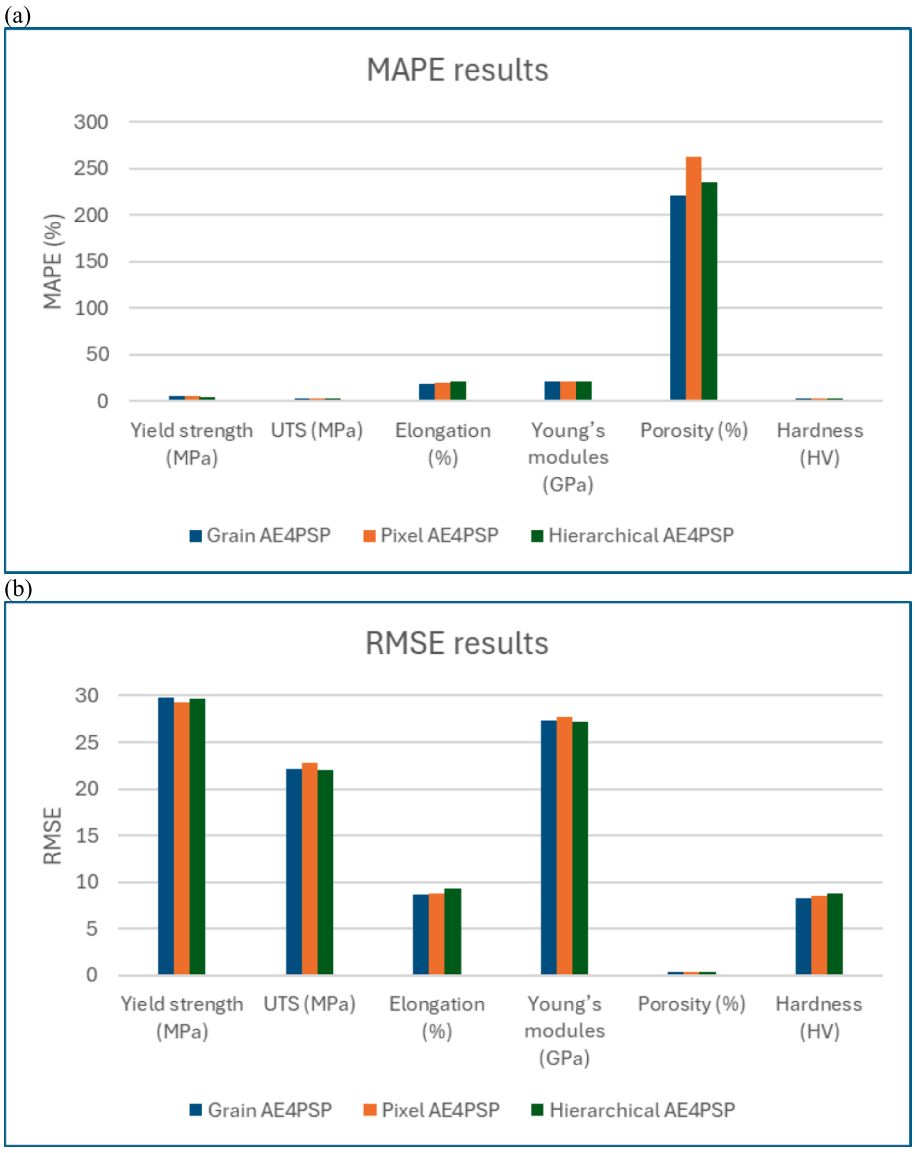

Fig. 10. Results (a) MAPE, (b) RMSE.

microstructure representations are learned comparably from grain-wise, pixel-wise, and hierarchical graphs. The MAPE for predictions of yield strength, UTS, and hardness are all below 5.2 %, whereas the MAPE for porosity exceeds 200 %. This discrepancy is due to the very small absolute value of porosity (less than 1.5 %), resulting in an RMSE for porosity as low as 0.3. For elongation and Young's modulus predictions, the MAPE is approximately 20 %.

The similar conclusion can be drawn from the plotted line chart in Fig. 11, which includes ± 5 % (darker grey bands) and ± 10 % (lighter grey bands) margins. The relative error percentages for predicting yield strength, tensile strength, and hardness fall within the 10 % band. The high relative error percentage for porosity prediction is due to the very small actual porosity values (less than 1.5 %). Despite this, the machine learning models can accurately follow the trend of porosity, with RMSE values being low (0.3 %). The predictions for elongation at break are within the normal range but fail to capture extreme values (less than 30 % and higher than 45 %). Similarly, the predictions for Young's modulus, ranging between 120 GPa and 140 GPa, adhere to the principle that Young's modulus is an inherent material property but do not account for experimental values below 100 GPa. The results indicate that the performance of models using pixel-wise and hierarchical graphs is nearly identical, as both approaches derive from pixel data without manual feature engineering. In contrast, the grain-wise graph, which involves manual feature engineering, shows slight deviations. The discrepancies observed between the model predictions and experimental results are primarily attributed to the smoothing effects inherent in machine learning models and experimental errors. The results demonstrate that anomalies, particularly the spikes, originate from experimental data. Outliers in elongation and Young's modulus are likely due to experimental errors or defects in the specimens. Therefore, further investigation into the experimental results for both elongation and Young's modulus is warranted.

What is more, the computational cost of training contrastive learning based on entire set of hierarchical graphs of EBSD microstructures also has been considered in our study. The initial idea is to convert each pixel into a graph node aligned with the EBSD data acquisition process without manual feature engineering, forming a pixel-wise graph. However, due to the millions of graph nodes, training is extremely slow. As shown in Table 8, PGCL is the most resource intensive. It uses the most CPU time (38 h, 32 min, and 10 s) and memory (about 13.56 GB). It also requires the highest amount of virtual memory at approximately 77.82 GB. To address this, a hierarchical graph was proposed to enable parallel training of smaller pixel-wise graphs converted from the pixels within each grain. HGCL uses 1 h, 10 min, and 33 s of CPU time, consumes

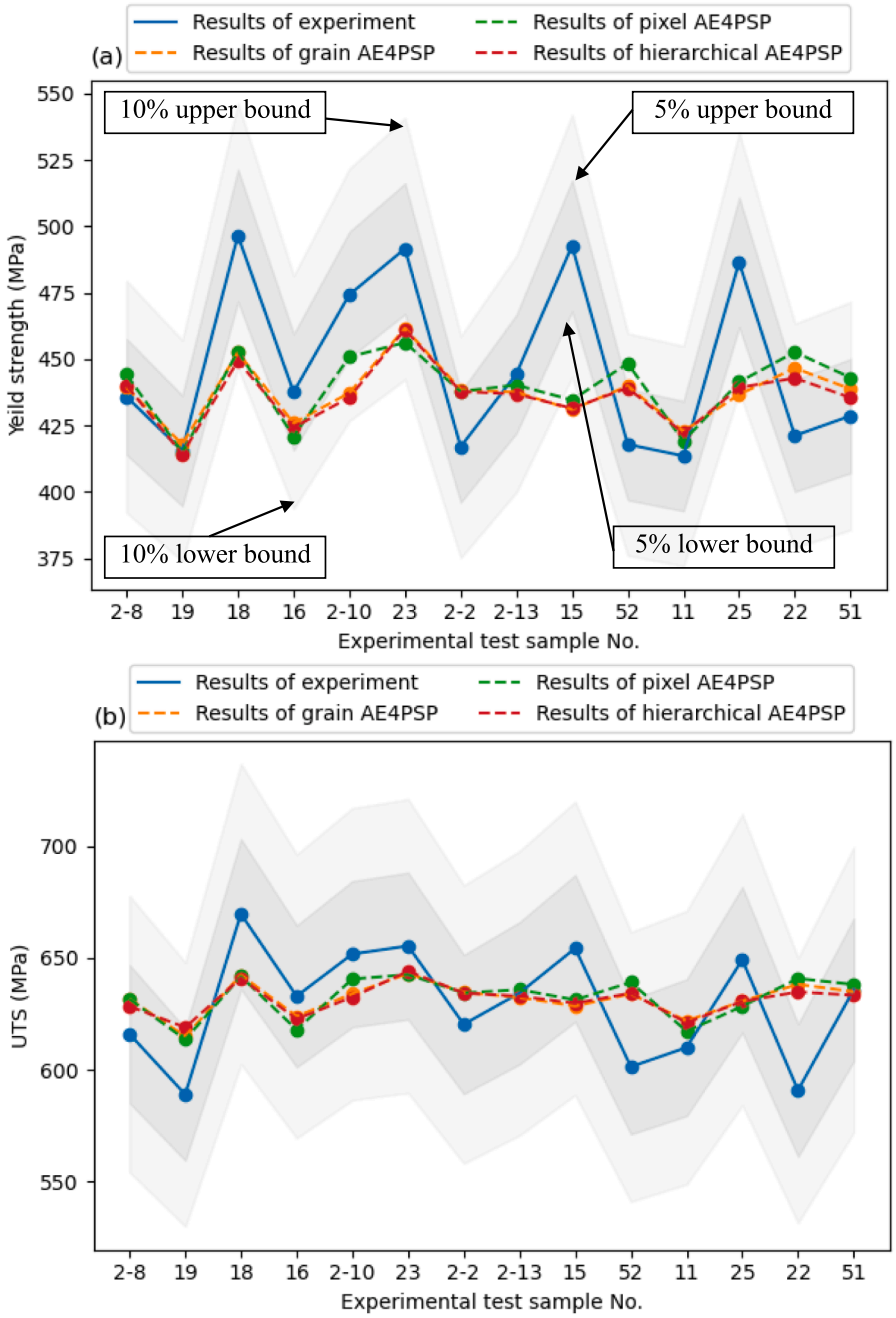

Fig. 11. Prediction results of AE4PSP (a) Tensile strength, (b) UTS, (c) Elongation at break, (d) Young's modules (e) Porosity (f) Hardness.

around 6.69 GB of memory, and uses about 57.23 GB of virtual memory. Furthermore, with manual feature engineering (selecting grain features through AZtecCrystal grain processing), grain-wise graphs are created. This reduces the number of graph nodes from millions to thousands, significantly speeding up the training process by eliminating the need for feature learning from pixel-wise graphs within grains. GGCL is the most efficient in terms of both CPU time and memory usage. It uses 4 min and 42 s of CPU time, consumes approximately 2.56 GB of memory, and uses around 15.62 GB of virtual memory. In summary, the PGCL model requires the most resources in terms of CPU time, memory, and virtual memory. The GGCL is the least resource-intensive, while the HGCL falls in between.

7. Conclusion and future work

In this study, an innovative algorithm is developed to transform microstructures to hierarchical graphs, preserving essential measurement data and structural details for training machine learning models. After that, a HGCL model is proposed for representation of microstructures obtained by EBSD technique. This model can be directly extended for other microscopy techniques, such as SEM, EDX, and TEM. By the learned microstructure representations, an autoencoder model for DED process is proposed to establish the relationship among process parameters (laser power, scanning speed, powder mass flow rate, XY-incremental ratio, Z-incremental ratio), microstructures, and material properties (yield strength, ultimate tensile strength, elongation at break, Young's modules, porosity, and hardness). The present model not only

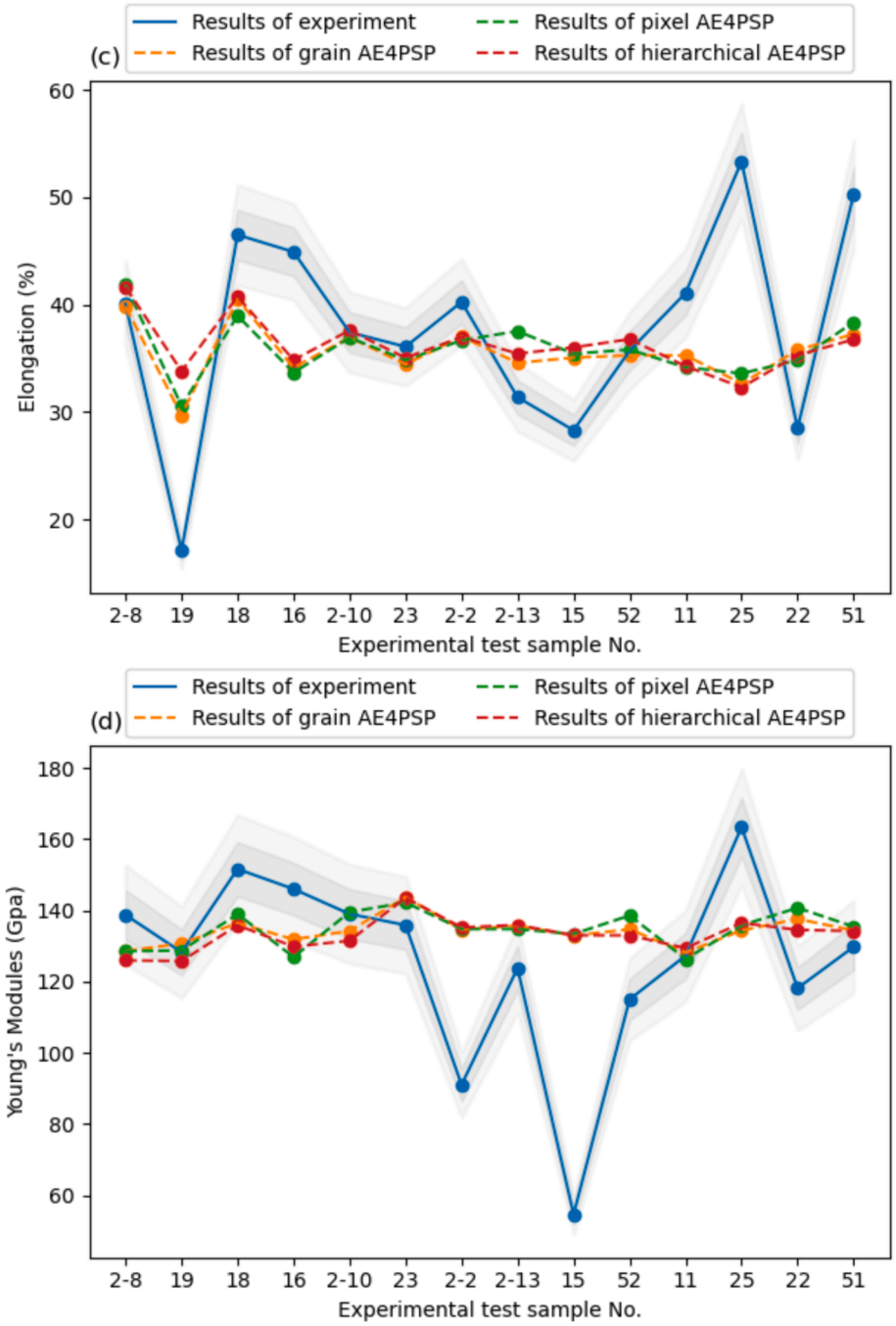

Fig. 11. (*continued*).

provides fundamental insights but also conduct a process-structure–property forward loop quantitatively, ensuring continuous material refinement.

One of the main limitations of the current research are the small dataset size limits the generalizability of the findings and the inability to decode the microstructures from the representation. Furthermore, the absence of a direct method to evaluate the performance of the representation learning of microstructure poses a limitation on the interpretability. Lastly, the high computational cost associated with the representation learning of microstructures, particularly without the use of manual feature engineering, is another significant limitation.

In future work, expanding the dataset to enhance the robustness of conclusions and being able to reconstruct or decode the microstructures from the learned representations would offer more insights into what the model has learned and how it can be manipulated or applied in novel ways can address first two limitations. Neighbor sampling algorithms in data preparation stage can be applied to HGCL for further developing efficient and scalable GNN.

CRediT authorship contribution statement

Chengxi Chen: Writing – original draft, Visualization, Validation, Software, Methodology, Investigation, Formal analysis, Data curation, Conceptualization. **Stanley Jian Liang Wong:** Writing – review & editing, Validation. **Eddie Zhi'En Tan:** . **Hua Li:** Writing – review & editing, Supervision, Project administration, Funding acquisition.

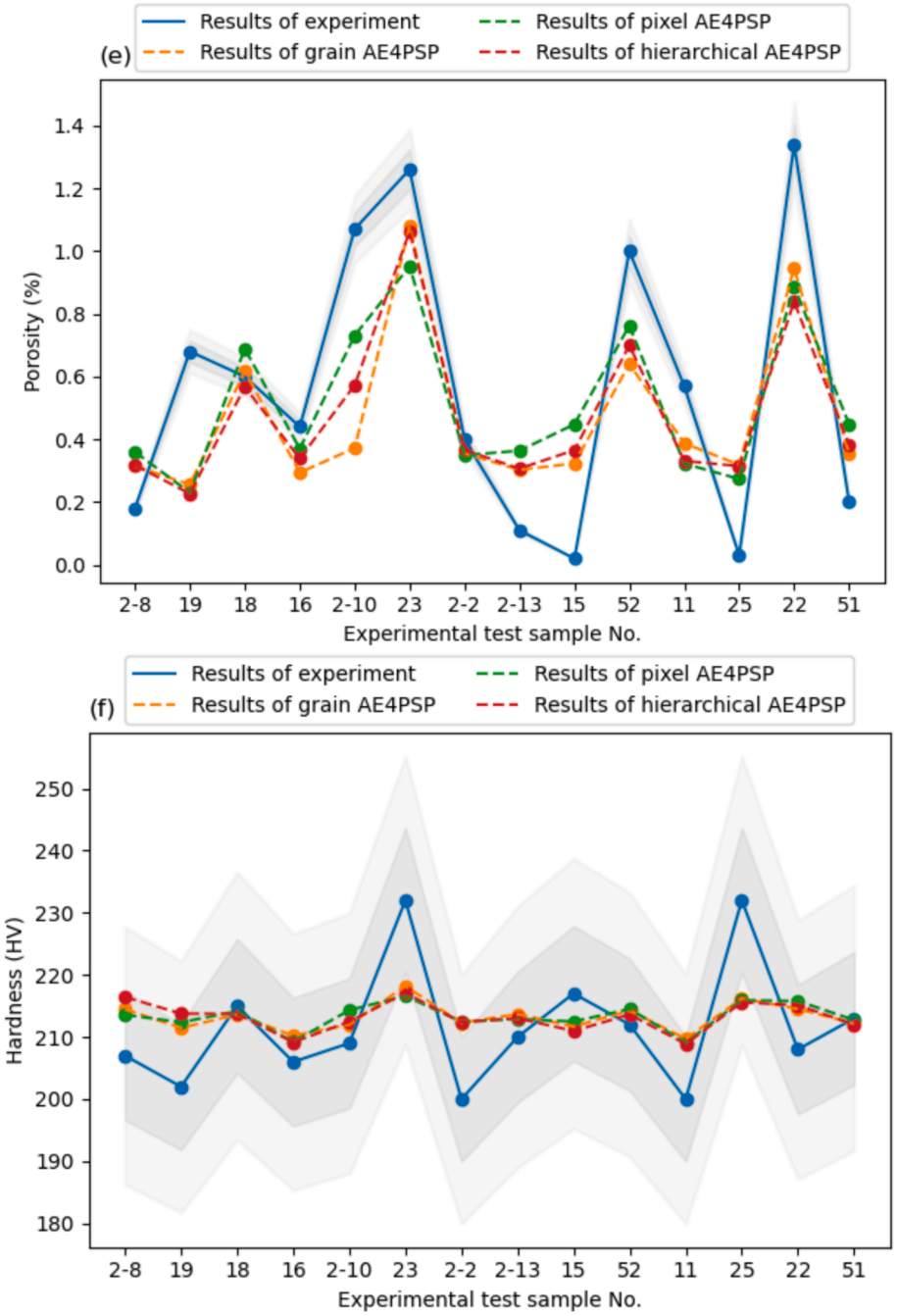

Fig. 11. (*continued*).

Table 8
Usage of computational resource.

Models	CPU time (hh: mm: ss)	Memory (kb)	Virtual memory (kb)
GGCL	00:04:42	2,558,984	15,620,704
PGCL	38:32:10	13,561,788	77,824,884
HGCL	01:10:33	6,686,948	57,225,012

Declaration of competing interest

The authors declare that they have no known competing financial interests or personal relationships that could have appeared to influence the work reported in this paper.

Data availability

Data will be made available on request.

Acknowledgments

This research is supported by Makino Asia Pte Ltd through the Economic Development Board Industrial Postgraduate Programme, and it is also backed by the National Research Foundation, Prime Minister's

Office, Singapore, under its Medium-Sized Centre funding scheme. Furthermore, this endeavor has been facilitated by the Singapore Centre for 3D Printing at Nanyang Technological University, Singapore, through the utilization of its additive manufacturing facilities. Additionally, we extend our gratitude to the Facility for Analysis, Characterization, Testing, and Simulation at Nanyang Technological University, Singapore, for granting access to their electron microscopy/X-ray facilities. All computational tasks related to this article were diligently executed utilizing the resources at the National Supercomputing Centre, Singapore (https://www.nscc.sg). Lastly, our profound appreciation goes to Dr. Yoshinari Yosuke from Makino Milling Machine Co., Ltd for his invaluable insights and discussions pertaining to the project.

Appendix A. Supplementary data

Supplementary data to this article can be found online at https://doi.org/10.1016/j.matdes.2024.113115.

References

[1] S.M. Thompson, L. Bian, N. Shamsaei, A. Yadollahi, An overview of Direct Laser Deposition for additive manufacturing; Part I: Transport phenomena, modeling and diagnostics, Addit. Manuf. 8 (2015) 36–62, https://doi.org/10.1016/j.addma.2015.07.001.

[2] B. Chen *et al.*, "Effect of Laser Beam Profile on Thermal Transfer, Fluid Flow and Solidification Parameters during Laser-Based Directed Energy Deposition of Inconel 718," *Materials (Basel).*, vol. 16, no. 12, 2023, doi: 10.3390/ma16124221.

[3] D.-G. Ahn, Directed Energy Deposition (DED) Process: State of the Art, Int. J. Precis. Eng. Manuf. Technol. 8 (2) (2021) 703–742, https://doi.org/10.1007/s40684-020-00302-7.

[4] N. Shamsaei, A. Yadollahi, L. Bian, S.M. Thompson, An overview of Direct Laser Deposition for additive manufacturing; Part II: Mechanical behavior, process parameter optimization and control, Addit. Manuf. 8 (2015) 12–35, https://doi.org/10.1016/j.addma.2015.07.002.

[5] A. Dass and A. Moridi, "State of the art in directed energy deposition: From additive manufacturing to materials design," *Coatings*, vol. 9, no. 7, 2019, doi: 10.3390/COATINGS9070418.

[6] T. Gatsos, K.A. Elsayed, Y. Zhai, D.A. Lados, Review on Computational Modeling of Process – Microstructure – Property Relationships in Metal Additive Manufacturing, JOM 72 (1) (2020) 403–419, https://doi.org/10.1007/s11837-019-03913-x.

[7] T. Debroy, et al., Progress in Materials Science Additive manufacturing of metallic components – Process, structure and properties, Prog. Mater. Sci. 92 (2018) 112–224, https://doi.org/10.1016/j.pmatsci.2017.10.001.

[8] T. Petrat, C. Brunner-Schwer, B. Graf, and M. Rethmeier, "Microstructure of Inconel 718 parts with constant mass energy input manufactured with direct energy deposition," in *17TH NORDIC LASER MATERIALS PROCESSING CONFERENCE (NOLAMP17)*, O. M. Akselsen and I. Bunaziv, Eds., 2019, pp. 256–266. doi: 10.1016/j.promfg.2019.08.033.

[9] M. Froend, V. Ventzke, S. Riekehr, N. Kashaev, B. Klusemann, J. Enz, Microstructure and microhardness of wire-based laser metal deposited AA5087 using an Ytterbium fibre laser, Mater. Charact. 143 (April) (2018) 59–67, https://doi.org/10.1016/j.matchar.2018.05.022.

[10] S. Bhattacharya, G.P. Dinda, A.K. Dasgupta, H. Natu, B. Dutta, J. Mazumder, Microstructural evolution and mechanical, and corrosion property evaluation of Cu-30Ni alloy formed by Direct Metal Deposition process, J. Alloys Compd. 509 (22) (Feb. 2011) 6364–6373, https://doi.org/10.1016/j.jallcom.2011.03.091.

[11] I.S. Loginova, et al., Peculiarities of the Microstructure and Properties of Parts Produced by the Direct Laser Deposition of 316L Steel Powder, Russ. J. Non-Ferrous Met. 60 (1) (2019) 87–94, https://doi.org/10.3103/S1067821219010085.

[12] E. Nyoni, E.T. Akinlabi, Process parameter interaction effect on the evolving properties of laser metal deposited titanium for biomedical applications, Thin Solid Films 620 (Feb. 2016) 94–102, https://doi.org/10.1016/j.tsf.2016.09.060.

[13] D.S. Shim, G.Y. Baek, J.S. Seo, G.Y. Shin, K.P. Kim, K.Y. Lee, Effect of layer thickness setting on deposition characteristics in direct energy deposition (DED) process, Opt. Laser Technol. 86 (2016) 69–78, https://doi.org/10.1016/j.optlastec.2016.07.001.

[14] T. Yu, Y. Zhao, J. Sun, Y. Chen, W. Qu, Process parameters optimization and mechanical properties of forming parts by direct laser fabrication of YCF101 alloy, J. Mater. Process. Technol. 262 (June) (2018) 75–84, https://doi.org/10.1016/j.jmatprotec.2018.06.023.

[15] C.C.C. Lesko, L.C. Sheridan, J.E. Gockel, Microhardness as a Function of Process Parameters in Additively Manufactured Alloy 718, J. Mater. Eng. Perform. 30 (9) (2021) 6630–6639, https://doi.org/10.1007/s11665-021-05938-3.

[16] R.M. Mahamood, E.T. Akinlabi, Scanning speed and powder flow rate influence on the properties of laser metal deposition of titanium alloy, Int. J. Adv. Manuf. Technol. 91 (5–8) (Jul. 2017) 2419–2426, https://doi.org/10.1007/s00170-016-9954-9.

[17] V.K. Balla, M. Das, A. Mohammad, A.M. Al-Ahmari, Additive Manufacturing of -TiAl: Processing, Microstructure, and Properties, Adv. Eng. Mater. 18 (7) (Jul. 2016) 1208–1215, https://doi.org/10.1002/adem.201500588.

[18] T. Bhardwaj, M. Shukla, C.P. Paul, K.S. Bindra, Direct Energy Deposition - Laser Additive Manufacturing of Titanium-Molybdenum alloy: Parametric studies, microstructure and mechanical properties, J. Alloys Compd. 787 (2019) 1238–1248, https://doi.org/10.1016/j.jallcom.2019.02.121.

[19] K.-W. Kim, G.-S. Ham, S.-H. Park, J.-W. Cho, K.-A. Lee, Direct energy deposition of ultrastrong WC-12Co cemented carbide: Fabrication, microstructure and compressive properties, Int. J. Refract. Metals Hard Mater. 99 (Sep. 2021), https://doi.org/10.1016/j.ijrmhm.2021.105591.

[20] T. Amine, J.W. Newkirk, F. Liou, Investigation of effect of process parameters on multilayer builds by direct metal deposition, Appl. Therm. Eng. 73 (1) (2014) 500–511, https://doi.org/10.1016/j.applthermaleng.2014.08.005.

[21] Q. Li, et al., Process, microstructure and microhardness of GH3039 superalloy processed by laser metal wire deposition, J. Alloys Compd. 877 (Oct. 2021), https://doi.org/10.1016/j.jallcom.2021.160330.

[22] J.-C. Zhang, Y.-P. Cao, H. Wang, T. Shi, B.-Y. Su, G.-R. Hua, Annular laser metal deposition of Ti-6Al-4V alloy in a semi-open environment: Process optimization, microstructure and mechanical properties, Optik (stuttg) 286 (Sep. 2023), https://doi.org/10.1016/j.ijleo.2023.171014.

[23] A. Whitt, et al., A process optimization framework for laser direct energy deposition: Densification, microstructure, and mechanical properties of an Fe-Cr alloy, J. Manuf. Process. 85 (Jan. 2023) 434–449, https://doi.org/10.1016/j.jmapro.2022.11.028.

[24] M. Rappaz, Modelling of microstructure formation in solidification processes, Int. Mater. Rev. 34 (1) (1989) 93–124, https://doi.org/10.1179/imr.1989.34.1.93.

[25] Z. Sun, W. Guo, L. Li, Numerical modelling of heat transfer, mass transport and microstructure formation in a high deposition rate laser directed energy deposition process, Addit. Manuf. 33 (Feb. 2020), https://doi.org/10.1016/j.addma.2020.101175.

[26] Y. Ji, L. Chen, and L. Q. Chen, *Understanding Microstructure Evolution During Additive Manufacturing of Metallic Alloys Using Phase-Field Modeling*, 1st ed. Elsevier Inc., 2018. doi: 10.1016/B978-0-12-811820-7.00008-2.

[27] W. Kurz, D.J. Fisher, R. Trivedi, Progress in modelling solidification microstructures in metals and alloys: dendrites and cells from 1700 to 2000, Int. Mater. Rev. 64 (6) (2019) 311–354, https://doi.org/10.1080/09506608.2018.1537090.

[28] F. K. Mirzade, "A phase field study of stress effects on microstructure formation during laser-aided direct metal deposition process," *Model. Asp. Opt. Metrol. VI*, vol. 10330, no. June 2017, p. 103301C, 2017, doi: 10.1117/12.2270122.

[29] D.J. Jarvis, Modelling of non-equilibrium solidification in ternary alloys: Comparison of ID, 2D, and 3D cellular automaton-finite difference simulations, Mater. Sci. Technol. 16 (11–12) (2000) 1420–1424, https://doi.org/10.1179/026708300101507389.

[30] T.F. Flint, Y.L. Sun, Q. Xiong, M.C. Smith, J.A. Francis, Phase-Field Simulation of Grain Boundary Evolution In Microstructures Containing Second-Phase Particles with Heterogeneous Thermal Properties, Sci. Rep. 9 (1) (2019) 1–11, https://doi.org/10.1038/s41598-019-54883-8.

[31] R.W. Geng, "multiscale Modeling of Microstructural Evolution in Fused-Coating Additive Manufacturing" 28 (October) (2019) 6544–6553, https://doi.org/10.1007/s11665-019-04375-7.

[32] N. Moelans, B. Blanpain, P. Wollants, An introduction to phase-field modeling of microstructure evolution, Calphad Comput. Coupling Phase Diagrams Thermochem. 32 (2) (2008) 268–294, https://doi.org/10.1016/j.calphad.2007.11.003.

[33] J. Akram, P. Chalavadi, D. Pal, B. Stucker, Understanding grain evolution in additive manufacturing through modeling, Addit. Manuf. 21 (May 2018) 255–268, https://doi.org/10.1016/j.addma.2018.03.021.

[34] Y. Lian, Z. Gan, C. Yu, D. Kats, W. Kam, G.J. Wagner, A cellular automaton finite volume method for microstructure evolution during additive manufacturing, Mater. Des. 169 (2019) 107672, https://doi.org/10.1016/j.matdes.2019.107672.

[35] C. Kumara *et al.*, "Microstructure modelling of laser metal powder directed energy deposition of alloy 718," *Addit. Manuf.*, vol. 25, no. August 2018, pp. 357–364, 2019, doi: 10.1016/j.addma.2018.11.024.

[36] R. Bostanabad, et al., Computational microstructure characterization and reconstruction: Review of the state-of-the-art techniques, Prog. Mater. Sci. 95 (2018) 1–41, https://doi.org/10.1016/j.pmatsci.2018.01.005.

[37] A.M. Kamara, S. Marimuthu, L. Li, Finite element modeling of microstructure in laser-deposited multiple layer inconel 718 parts, Mater. Manuf. Process. 29 (10) (2014) 1245–1252, https://doi.org/10.1080/10426914.2014.930963.

[38] X. Zhan, Y. Meng, J. Zhou, C. Qi, C. Zhang, D. Gu, Quantitative research on microstructure and thermal physical mechanism in laser melting deposition for Invar alloy, J. Manuf. Process. 31 (Jan. 2018) 221–231, https://doi.org/10.1016/j.jmapro.2017.11.018.

[39] X. Lin, T.M. Yue, H.O. Yang, W.D. Huang, Microstructure and phase evolution in laser rapid forming of a functionally graded Ti-Rene88DT alloy, Acta Mater. 54 (7) (2006) 1901–1915, https://doi.org/10.1016/j.actamat.2005.12.019.

[40] Y. Lian, Z. Gan, C. Yu, D. Kats, W.K. Liu, G.J. Wagner, A cellular automaton finite volume method for microstructure evolution during additive manufacturing, Mater. Des. 169 (2019) 107672, https://doi.org/10.1016/j.matdes.2019.107672.

[41] T. Xue, Z. Gan, S. Liao, J. Cao, Physics-embedded graph network for accelerating phase-field simulation of microstructure evolution in additive manufacturing, Npj Comput. Mater. 8 (1) (2022) pp, https://doi.org/10.1038/s41524-022-00890-9.

[42] M. Alimardani, C.P. Paul, E. Toyserkani, A. Khajepour, Multiphysics modelling of laser solid freeform fabrication techniques, Adv. Laser Mater. Process. (2010) 765–791, https://doi.org/10.1533/9781845699819.8.765.
[43] Z.J. Wang, S. Luo, H.W. Song, W.D. Deng, W.Y. Li, Simulation of Microstructure during Laser Rapid Forming Solidification Based on Cellular Automaton, Math. Probl. Eng. 2014 (2014), https://doi.org/10.1155/2014/627528.
[44] M. Rappaz, C.A. Gandin, Probabilistic modelling of microstructure formation in solidification processes, Acta Metall. Mater. 41 (2) (1993) 345–360, https://doi.org/10.1016/0956-7151(93)90065-Z.
[45] S. Safdar, A.J. Pinkerton, L. Li, M.A. Sheikh, P.J. Withers, An anisotropic enhanced thermal conductivity approach for modelling laser melt pools for Ni-base super alloys, Appl. Math. Model. 37 (3) (Feb. 2013) 1187–1195, https://doi.org/10.1016/j.apm.2012.03.028.
[46] A. V. Dubrov, F. K. Mirzade, and V. D. Dubrov, "On multi-scale modelling of dendrite growth during laser metal deposition process," vol. 1067514, no. May 2018, p. 40, 2018, doi: 10.1117/12.2307555.
[47] Y. Shimono, M. Oba, S. Nomoto, Solidification simulation of direct energy deposition process by multi-phase field method coupled with thermal analysis, Model. Simul. Mater. Sci. Eng. 27 (7) (2019), https://doi.org/10.1088/1361-651X/ab3433.
[48] C. Herriott, et al., A multi-scale, multi-physics modeling framework to predict spatial variation of properties in additive-manufactured metals, Model. Simul. Mater. Sci. Eng. 27 (2) (2019), https://doi.org/10.1088/1361-651X/aaf753.
[49] J. Irwin, *Modeling Microstructure of AM Processes Using the FE Method*, 1st ed., vol. 138, no. 11. Elsevier Inc., 2017. doi: 10.1016/B978-0-12-811820-7.00009-4.
[50] P. Nath, Z. Hu, S. Mahadevan, Uncertainty quantification of grain morphology in laser direct metal deposition, Model. Simul. Mater. Sci. Eng. 27 (4) (Jun. 2019), https://doi.org/10.1088/1361-651X/ab1676.
[51] K. Ren, Y. Chew, Y. F. Zhang, J. Y. H. Fuh, and G. J. Bi, "Thermal field prediction for laser scanning paths in laser aided additive manufacturing by physics-based machine learning," *Comput. Methods Appl. Mech. Eng.*, vol. 362, no. SI, Apr. 2020, doi: 10.1016/j.cma.2019.112734.
[52] N. Shamsaei, A. Yadollahi, L. Bian, and S. M. Thompson, "An overview of Direct Laser Deposition for additive manufacturing; Part II: Mechanical behavior, process parameter optimization and control," *Additive Manufacturing*, vol. 8. Elsevier B.V., pp. 12–35, Oct. 01, 2015. doi: 10.1016/j.addma.2015.07.002.
[53] W. Yan, et al., Modeling process-structure-property relationships for additive manufacturing, Front. Mech. Eng. 13 (4) (2018) 482–492, https://doi.org/10.1007/s11465-018-0505-y.
[54] W. Yan, et al., An integrated process–structure–property modeling framework for additive manufacturing, Comput. Methods Appl. Mech. Eng. 339 (2018) 184–204, https://doi.org/10.1016/j.cma.2018.05.004.
[55] J. Li, M. Sage, X. Guan, M. Brochu, Y.F. Zhao, Machine Learning-Enabled Competitive Grain Growth Behavior Study in Directed Energy Deposition Fabricated Ti6Al4V, Jom 72 (1) (2020) 458–464, https://doi.org/10.1007/s11837-019-03917-7.
[56] Y. Han, R.J. Griffiths, H.Z. Yu, Y. Zhu, Quantitative microstructure analysis for solid-state metal additive manufacturing via deep learning, J. Mater. Res. 35 (15) (2020) 1936–1948, https://doi.org/10.1557/jmr.2020.120.
[57] A. Gayon-Lombardo, L. Mosser, N.P. Brandon, S.J. Cooper, "Pores for thought: generative adversarial networks for stochastic reconstruction of 3D multi-phase electrode microstructures with periodic boundaries", *npj Comput*, Mater. 6 (1) (2020) 82, https://doi.org/10.1038/s41524-020-0340-7.
[58] S. Kench, S.J. Cooper, Generating three-dimensional structures from a two-dimensional slice with generative adversarial network-based dimensionality expansion, Nat. Mach. Intell. 3 (2021) 299–305, https://doi.org/10.1038/s42256-021-00322-1.
[59] L. Fang, L. Cheng, J.A. Glerum, J. Bennett, J. Cao, G.J. Wagner, "Data-driven analysis of process, structure, and properties of additively manufactured Inconel 718 thin walls", *npj Comput*, Mater. 8 (1) (2022) 1–15, https://doi.org/10.1038/s41524-022-00808-5.
[60] ASTM International, "Standard Test Methods for Tension Testing of Metallic Materials," West Conshohocken, PA, 2022. doi: 10.1520/E0008_E0008M-22.
[61] A.N. Jinoop, C.P. Paul, K.S. Bindra, Laser-assisted directed energy deposition of nickel super alloys: A review, Proc. Inst. Mech. Eng. PART L-JOURNAL Mater. Appl. 233 (11) (Nov. 2019) 2376–2400, https://doi.org/10.1177/1464420719852658.
[62] K. Xu, W. Hu, J. Leskovec, S. Jegelka, How Powerful are Graph Neural Networks? [Online].Available: ArXiv vol. abs/1810.00826 (2018) https://api.semanticscholar.org/CorpusID:52895589.
[63] X. Chen, K. He, "Exploring Simple Siamese Representation Learning", in, IEEE/CVF Conference on Computer Vision and Pattern Recognition (CVPR) 2021 (2021) 15745–15753, https://doi.org/10.1109/CVPR46437.2021.01549.
[64] C. Chen, S.J.L. Wong, S. Raghavan, H. Li, Design of experiments informed deep learning for modeling of directed energy deposition process with a small-size experimental dataset, Mater. Des. 222 (2022) 111098, https://doi.org/10.1016/j.matdes.2022.111098.